



# Analysis of a mesoscale infiltration and water seepage test in unsaturated fractured rock: Spatial variabilities and discrete fracture patterns

Quanlin Zhou <sup>a,\*</sup>, Rohit Salve <sup>a</sup>, Hui-Hai Liu <sup>a</sup>,  
Joseph S.Y. Wang <sup>a</sup>, David Hudson <sup>b</sup>

<sup>a</sup> Earth Sciences Division, Lawrence Berkeley National Laboratory,  
University of California, Berkeley, CA 94720, United States

<sup>b</sup> U.S. Geological Survey, Las Vegas, NV 89144, United States

Received 7 May 2004; received in revised form 13 April 2006; accepted 4 May 2006

Available online 21 June 2006

## Abstract

A mesoscale (21 m in flow distance) infiltration and seepage test was recently conducted in a deep, unsaturated fractured rock system at the crossover point of two underground tunnels. Water was released from a 3 m×4 m infiltration plot on the floor of an alcove in the upper tunnel, and seepage was collected from the ceiling of a niche in the lower tunnel. Significant temporal and (particularly) spatial variabilities were observed in both measured infiltration and seepage rates. To analyze the test results, a three-dimensional unsaturated flow model was used. A column-based scheme was developed to capture heterogeneous hydraulic properties reflected by these spatial variabilities observed. Fracture permeability and van Genuchten  $\alpha$  parameter [van Genuchten, M.T., 1980. A closed-form equation for predicting the hydraulic conductivity of unsaturated soils. *Soil Sci. Soc. Am. J.* 44, 892–898] were calibrated for each rock column in the upper and lower hydrogeologic units in the test bed. The calibrated fracture properties for the infiltration and seepage zone enabled a good match between simulated and measured (spatially varying) seepage rates. The numerical model was also able to capture the general trend of the highly transient seepage processes through a discrete fracture network. The calibrated properties and measured infiltration/seepage rates were further compared with mapped discrete fracture patterns at the top and bottom boundaries. The measured infiltration rates and calibrated fracture permeability of the upper unit were found to be partially controlled by the fracture patterns on the infiltration plot (as indicated by their positive correlations with fracture density). However, no correlation could be established between measured seepage rates and density of fractures mapped on the niche ceiling. This lack of correlation indicates the

\* Corresponding author.

E-mail addresses: [Qlzhou@lbl.gov](mailto:Qlzhou@lbl.gov) (Q. Zhou), [R\\_Salve@lbl.gov](mailto:R_Salve@lbl.gov) (R. Salve), [HHliu@lbl.gov](mailto:HHliu@lbl.gov) (H.-H. Liu), [JSWang@lbl.gov](mailto:JSWang@lbl.gov) (J.S.Y. Wang), [dhudson@usgs.gov](mailto:dhudson@usgs.gov) (D. Hudson).

complexity of (preferential) unsaturated flow within the discrete fracture network. This also indicates that continuum-based modeling of unsaturated flow in fractured rock at mesoscale or a larger scale is not necessarily conditional explicitly on discrete fracture patterns.

© 2006 Elsevier B.V. All rights reserved.

*Keywords:* Unsaturated flow; Fractured rock; Numerical modeling; Heterogeneity; Infiltration; Seepage; Field test

## 1. Introduction

Unsaturated flow in fractured rock has gained increasing attention in the past two decades, particularly in its application to geologic disposal of nuclear wastes and environmental contamination in arid and semi-arid regions (Bodvarsson and Tsang, 1999; Pruess, 1999; NRC, 2001; Bodvarsson et al., 2003). Unsaturated flow involves many complex physical and dynamic processes (e.g., Glass et al., 1995; Bodvarsson et al., 2003). This complexity results from heterogeneity within single fractures and fracture networks, nonlinearity in capillarity and relative permeability, fracture–matrix interactions, and contrast in hydraulic properties between fractures and the matrix (e.g., Zhou et al., 2003). Because of its complexity, the understanding of unsaturated flow in fractured rock, from small-scale mechanisms to large-scale processes, is still evolving (Tokunaga and Wan, 1997; Glass et al., 2002). At a large-scale, preferential flow along faults and large, actively connected fractures has been recognized as an important feature of water percolation. Evidence of large-scale preferential flow has been collected using environmental isotopes and applied tracers (Liu et al., 1995; Nativ et al., 1995; Fabryka-Martin et al., 1996; Yang et al., 1996). This preferential flow reduces the effective fracture–matrix interface area for flow and transport interaction, and enhances relative permeability for actively participating fractures. The performance of a large-scale fractured rock system is often evaluated by numerical analysis based on the continuum approach and site-specific fracture geometric properties (e.g., fracture spacing and density) collected from fracture mapping and outcrop studies. In the continuum approach, a fracture continuum and a single or multiple matrix continua are used to represent discrete fracture networks and the rock matrix, respectively (Barenblatt et al., 1960; Warren and Root, 1963; Pruess and Narasimhan, 1985).

Laboratory and field experiments for single fractures and small-scale fracture networks have been conducted to improve our understanding of unsaturated flow. A number of studies have noted that water flow within single fractures exhibits complicated physical processes and dynamic behavior, such as gravity-driven fingers, fragmented flow, flow diversion, and intermittent pulsations (e.g., Nicholl et al., 1994; Brown et al., 1998; Dahan et al., 1999; Su et al., 1999; Salve et al., 2004). Fingers result from the flow instability caused by Rayleigh processes and in-fracture-plane heterogeneity of fracture apertures, as found by many numerical simulations using spatially varying fracture aperture distributions (e.g., Bear et al., 1993). Recent field experiments conducted in a single fracture (Dahan et al., 1999) and a fault (Salve et al., 2004) demonstrated that flow follows complicated patterns, with strong spatial variabilities in infiltration and seepage rates. In fracture networks at a small-scale (on the order of meters), individual fractures and fracture intersections act as capillary barriers or flow integrators at different locations and times. Glass et al. (2002) conducted a field experiment by infiltrating dyed water, under ponded conditions, into a well-connected fracture network. During the excavation of the rock mass to a depth of 5 m, they mapped the fracture network and tracer distribution (the structure of the liquid phase) within a number of horizontal pavements immediately below the

infiltration surface. They found that with increasing depth, flow transitioned from pervasive patterns of viscous-force-dominated flow, to unsaturated flow with complex phase structures, such as fragmentation, preferential flow, fingers, irregular wetting patterns, and varied behavior at fracture intersections. These small-scale dynamic processes are difficult to characterize by both the continuum approach model and the discrete fracture network (DFN) model (e.g., [Cacas et al., 1990](#); [Dverstorp et al., 1992](#); [Therrien and Sudicky, 1996](#); [Ohman and Niemi, 2003](#)). The numerical analysis for small-scale experiments often focuses on the integrated response of unsaturated flow to system input, neglecting the spatial variability in observed flow rates (e.g., [Liu et al., 2003b](#)). With the internal structure of fractures unknown, the DFN model is often used with stochastically generated fracture patterns, and multiple realizations may be needed to characterize the uncertainties in the integrated flow features. In some cases, the available discrete fracture patterns may be used to explicitly project discrete fractures embedded within the matrix block (e.g., [Doughty, 2000](#); [Doughty et al., 2002](#)). However, the physical processes observed in the small-scale experiments and their numerical modeling may not be of particular relevance to a large-scale fractured rock system.

Between the large-scale (on the order of hundreds to thousands of meters) and the small-scale (on the order of meters) exists a mesoscale (on the order of tens of meters), whose physical processes and dynamic behavior are important for many practical applications (e.g., nuclear waste disposal and contamination remediation). Mesoscale processes of unsaturated flow in fractured rocks have been observed in few field experiments (e.g., [Faybishenko et al., 2000](#); [BSC, 2003a](#); [Liu et al., 2003b](#)). Recently, a mesoscale field test was conducted in a 21-m-thick unsaturated fractured rock ([Salve, 2005](#)). Spatial variabilities in measured infiltration and seepage rates were observed through a number of infiltration subplots at the top boundary and seepage collection locations at the bottom boundary. Maps of discrete fractures were also available at the top and bottom boundaries of the test bed. However, modeling these spatial variabilities in hydrologic responses is a big challenge, because previous modeling analysis has either focused on lumped infiltration or seepage by neglecting their spatial variabilities (e.g., [Doughty, 2000](#)), or captured the statistics of these spatial variabilities by using stochastically generated rock properties (e.g., [Finsterle et al., 2003](#)).

The objective of this paper is to develop a methodology to incorporate all data available on hydrologic responses, and discrete and continuum-based fracture and rock properties into modeling analysis. Are location-specific discrete fracture patterns essential to accurate simulation of mesoscale (or larger) unsaturated flow using the continuum-based approach? Do the rock properties calibrated using measured hydrologic responses represent mapped discrete fractures? To answer these questions and to develop a corresponding methodology, we (1) used a continuum-based numerical model to analyze the infiltration and seepage results of the test presented in [Salve \(2005\)](#), (2) developed the conceptual model of deterministic, column-based heterogeneity to capture the spatial variabilities in the measured infiltration and seepage rates, and (3) studied the correlations of discrete fracture patterns, mapped at the top and bottom boundaries of the test bed, with the measured hydrologic responses and calibrated rock properties.

## 2. Field testing

The mesoscale infiltration and seepage test evaluated in this study was conducted in the deep, unsaturated fractured rock at Yucca Mountain, Nevada, from August 20, 2002 to March 24, 2003. Water was released to an infiltration plot on the floor of an alcove (Alcove 8) and seepage was collected from the ceiling of a niche (Niche 3) located directly under the infiltration plot (see Fig.

1 in Salve, 2005). The test consisted of three distinct components for investigating the flow processes: (1) ponded release of water into infiltration subplots on the alcove floor, (2) collection of seepage from the niche ceiling, and (3) borehole monitoring of changes in fracture saturation and water potential. For the detailed test setup, the reader can refer to Salve (2005).

## 2.1. Geologic settings and rock properties

Niche 3 is approximately 4 m in width and 6.3 m in length. The total surface area of the niche ceiling is 16.4 m<sup>2</sup>. Niche 3 is located within the middle nonlithophysal unit (Tptpmn) of the Topopah Spring welded tuff (TSw). The Tptpmn unit (henceforth referred to as the “lower unit”) is a densely welded, highly fractured devitrified zone, containing few lithophysal cavities. Within this unit, fracture frequency varies significantly, with a mean value and a standard deviation of  $4.3 \pm 3.4 \text{ m}^{-1}$  (BSC, 2003c; Hinds et al., 2003). Alcove 8 is wider and longer than Niche 3, covering the entire area of the niche ceiling. The distance from the alcove floor to the niche ceiling is 21 m. Alcove 8 is situated within the upper lithophysal (Tptpul) unit of the TSw unit. The Tptpul unit (henceforth referred to as the “upper unit”) contains large, naturally occurring cavities (called lithophysae). Fractures appear to be the cooling features associated with lithophysae cavities. The mean and standard deviation of fracture frequency are  $0.8 \pm 1.0 \text{ m}^{-1}$ . Cavities and fractures in the upper unit lead to large effective fracture porosity, whose calibrated value (6.6%) is much larger

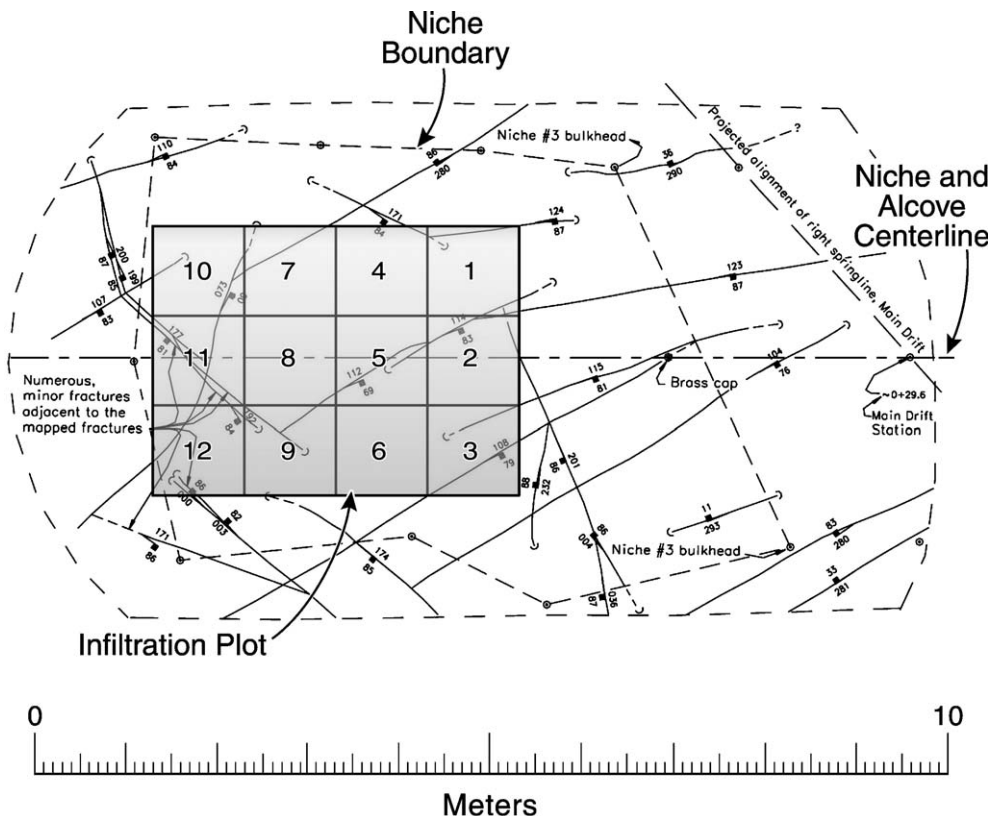


Fig. 1. Fracture map on the floor of Alcove 8 with configuration of the 12 infiltration subplots used for the test.



site is much less than that for the entire lower unit, indicating that Niche 3 is located in a moderately fractured zone of relatively low fracture density, as shown in the fracture density contour map (see Figure 3c in Wang and Bodvarsson, 2003).

In addition to the site-specific fracture geometric characteristics, fracture air permeability ( $k_f$  in  $m^2$ ) was also measured for each packed-off interval of 0.3 m along several boreholes around Niche 3 under both pre-excavation and post-excavation conditions, and along six near-vertical boreholes around Alcove 8 under post-excavation conditions (Cook, 2000; BSC, 2003a). The mean and standard deviation of log air permeability for the borehole cluster around Niche 3 are  $\log k_f = -13.4 \pm 0.70$  ( $\log m^2$ ) under pre-excavation conditions and  $-12.4 \pm 0.82$  ( $\log m^2$ ) under post-excavation conditions. This difference indicates that the post-excavation air permeability is one order of magnitude higher than the pre-excavation counterpart, most likely because of excavation-induced stress release (Wang and Elsworth, 1999). For the borehole cluster around Alcove 8, the air permeability data produces a mean and standard deviation:  $\log k_f = -13.1 \pm 1.29$  ( $\log m^2$ ). Matrix characteristics are fairly homogeneous within these two units (Flint, 1998a,b). The mean matrix permeability values for laboratory rock cores are nearly five orders of magnitude less than mean fracture permeability values in these two hydrogeologic units.

## 2.2. Infiltration test

A  $3\text{ m} \times 4\text{ m}$  infiltration plot was trenched on the floor of Alcove 8 (see Fig. 1). The plot was divided into 12 separated subplots of the same  $1\text{ m} \times 1\text{ m}$  area. Each subplot was connected to an individual permeameter through which water was applied. The water level in each subplot was maintained at a head of 2 cm. Fig. 3 shows the highly transient total infiltration rate (time) series (as a function of time), exhibiting a three-stage pattern. The total infiltration rate at a given time is defined by the overall infiltration rate through the entire plot. In the first stage, the infiltration rate reaches a high value of 644 l/day on the first day, then it decreases sharply over the following

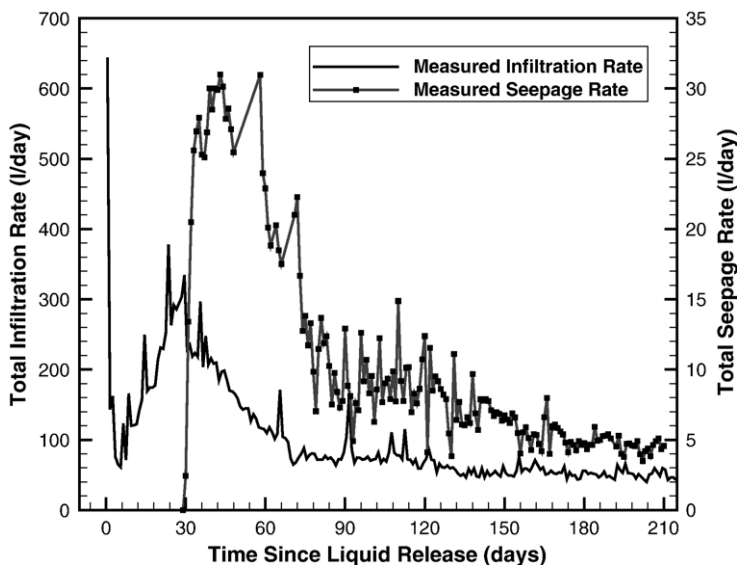


Fig. 3. Total infiltration rates (l/day) measured through the infiltration plot and total seepage rates (l/day) measured through the ceiling of Niche 3.



5 days. In the second stage, the rate increases steadily to a value of 334 l/day by the 29th day. In the third stage (from the 29th day to 215th day), the infiltration rate decreases sharply within the first 40 days, then it remains relatively stable, even though it continues to gradually decline. The maximum infiltration rate on the first day is about 13 times as large as that under quasi-stable conditions after 120 days of liquid release.

The strong spatial variability of infiltration rates is shown in Figs. 4 and 5. Fig. 4 shows the transient infiltration-rate series measured in each of the 12 infiltration subplots. The spatial variability of infiltration rates is observed in terms of the magnitude and transient pattern of infiltration rates through different subplots. A number of subplots share a transient three-stage infiltration pattern similar to the total infiltration rate; the other subplots have a relatively stable infiltration rate through the entire test period. As shown in Fig. 5, the normalized infiltration rates for the highly transient period (the first 90 days) and the quasi-steady-state period (the last 125 days) also vary significantly. The normalized infiltration rate for a subplot is obtained by dividing the mean infiltration rate of this subplot averaged over the first 90 days of high infiltration (or the later 125 days of low infiltration) by the mean total infiltration rate during the same period. For both early and later times, Subplot 2 with the highest normalized infiltration rates accounts for about 30% of the total infiltration rates, whereas Subplot 4 with the smallest normalized infiltration rate accounts for less than 1.5%; the sum of the normalized infiltration

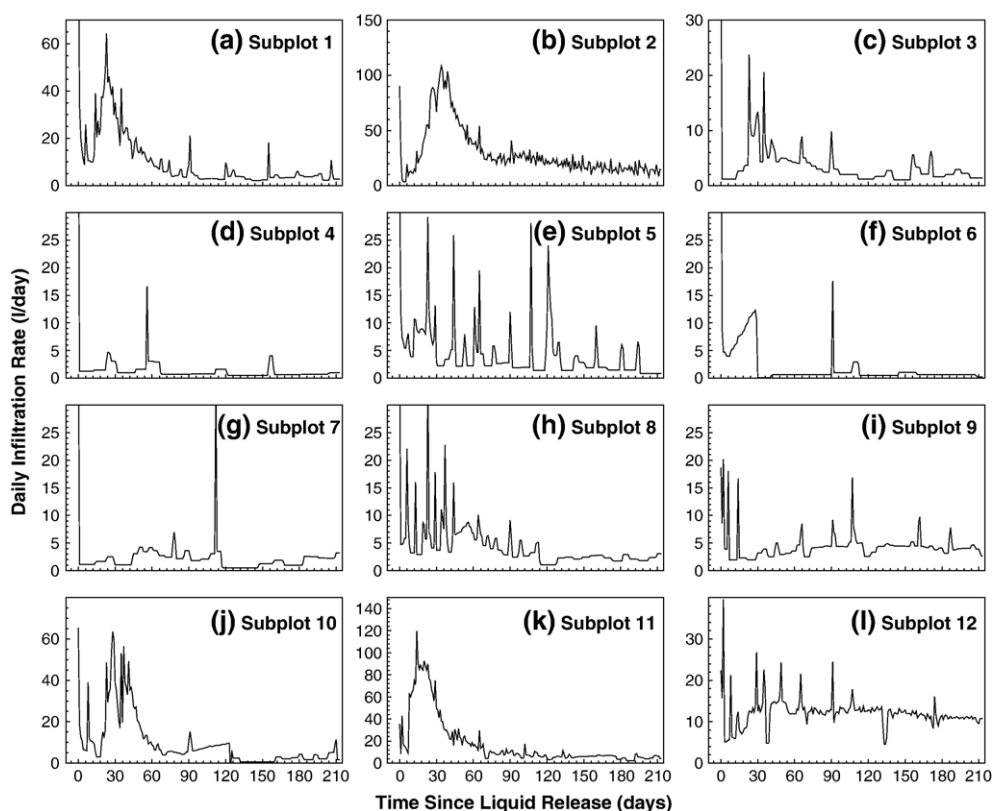


Fig. 4. Transient infiltration rates (l/day) measured at the 12 infiltration subplots located on the floor of Alcove 8.

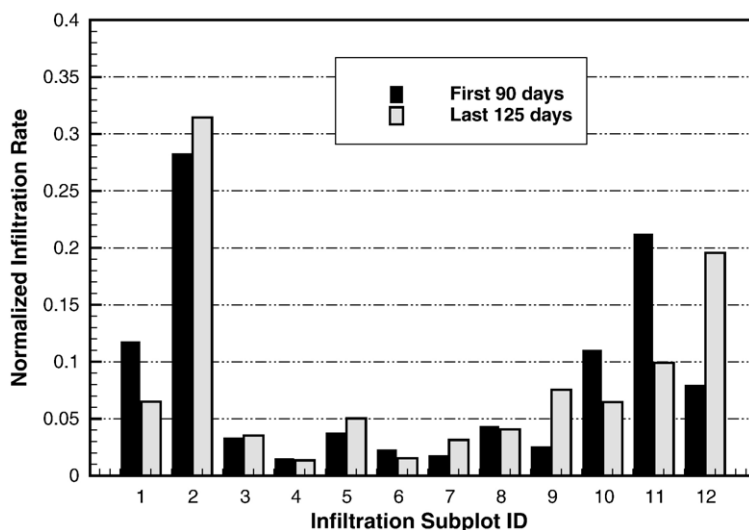


Fig. 5. Spatial variability of the normalized infiltration rates of the 12 subplots during the highly transient period (the first 90 days) and the quasi-steady-state period (the last 125 days).

rates in six subplots (Subplots 1, 2, 9, 10, 11, and 12) is approximately 81% of the total infiltration rates.

### 2.3. Seepage test

Seepage was collected at the ceiling of Niche 3 by a capture system having 11 tray units of different surface areas (see Fig. 2). An additional collection tray unit was used to collect seepage flowing along the niche's right wall. The total cross-sectional area of the capture system was 16.4 m<sup>2</sup>. Fig. 3 shows the total seepage rate measured for the 12 tray units, exhibiting strong temporal variability. Seepage occurs 30 days after liquid release. The seepage rate increases rapidly up to 30 l/day within 2–3 days, and then it remains relatively stable until it starts to decline significantly from 60 to 90 days after liquid release. After that, the seepage rate becomes relatively stable, and a quasi-steady state is reached. At the later quasi-steady-state time (the last 125 days), only 10% of the total volume of the liquid released from the entire infiltration plot on Alcove 8 seeps out of the fractured rock through the niche ceiling, and 90% of the total released liquid is stored in the fractured rock or flows away around the niche.

The seepage rates in different tray units reflected the spatial variability in the seepage on the niche ceiling. Fig. 6 shows the time series of seepage rates (l/day, per unit area of a subtray) measured for each of the 12 tray units. Note that at a given time, the seepage rate for an individual tray unit is obtained by dividing the collected seepage rate through this tray unit by its total number of subtray assemblies. A subtray assembly is of an area 0.3 m by 1.2 m (1 ft by 4 ft). Fig. 7 shows the spatial variability of the normalized seepage rate at the early highly transient time and the later quasi-steady-state time. The normalized seepage rate for a tray unit is obtained by dividing the mean seepage rate averaged over the early 90 days (or later 125 days) in the tray unit, by the mean total seepage rate during the same time period.



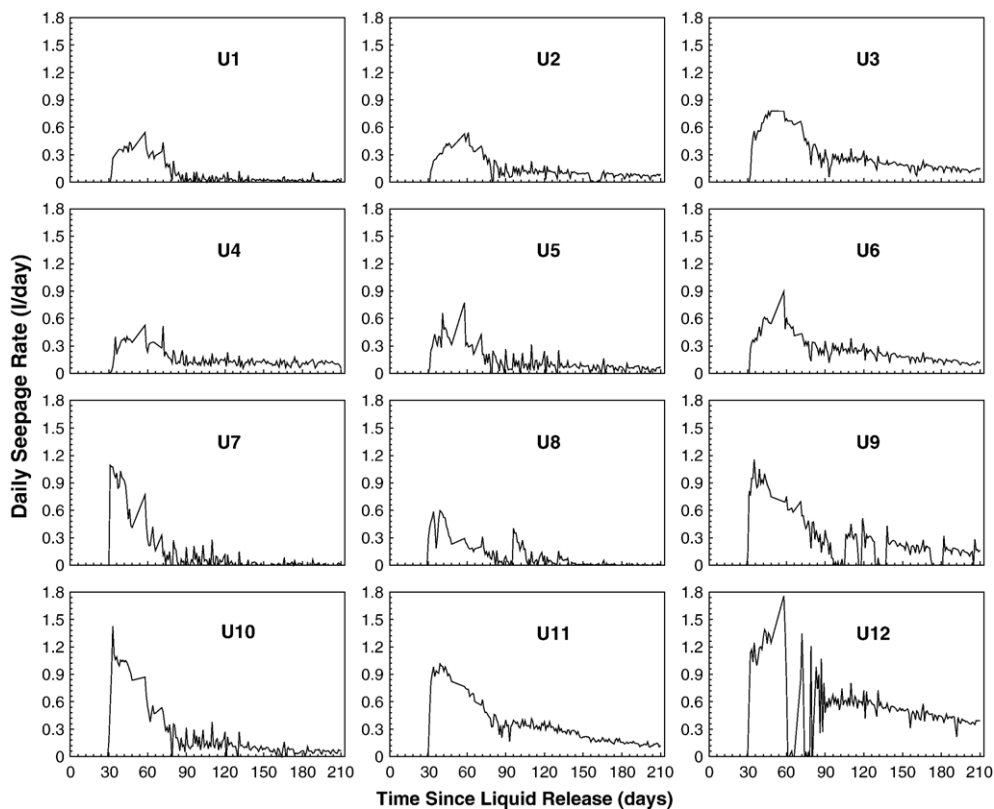


Fig. 6. Transient seepage rates (l/day), per unit area of a subtray (0.3 m × 1.2 m), measured for the 12 tray units at the ceiling of Niche 3.

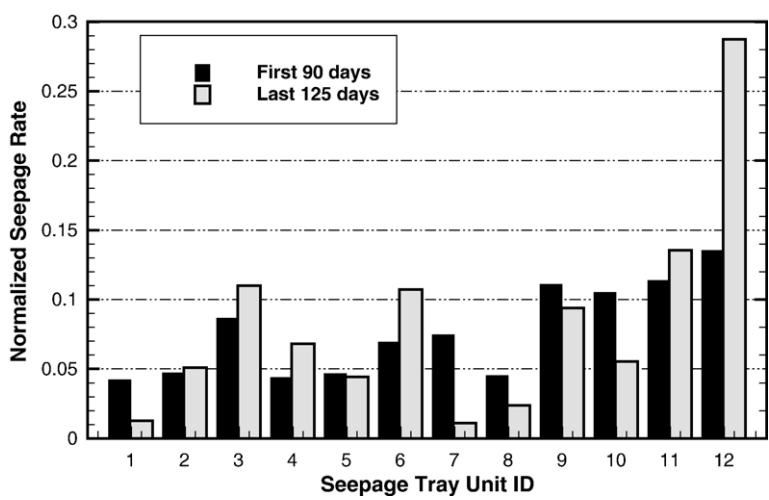


Fig. 7. Spatial variability of the normalized seepage rates during the highly transient period (the first 90 days) and the quasi-steady-state period (the last 125 days).

## 2.4. Travel time monitoring

Within the fractured rock, changes (with time) in saturation and potential of fracture water, along boreholes drilled around Niche 3, were monitored using electrical resistivity probes over the entire test period. A sharp drop in the electrical resistivity indicates an increase in fracture saturation, which is in turn representative of the wetting-front arrival of liquid flow within the fracture network (Salve et al., 2003; Salve, 2005). The travel time of wetting fronts, measured along three horizontal boreholes approximately 0.5 m above the niche ceiling, was fairly uniform for the entire ceiling. The travel time from the infiltration plot to the borehole sensors was  $\sim 29$  days.

## 3. Modeling analysis

To understand the infiltration and seepage processes presented in Section 2, we used a three-dimensional unsaturated flow model based on the continuum approach. To match the observed temporal and spatial variabilities, we developed the conceptual model of deterministic, column-based heterogeneity to represent the spatially varying rock properties. The numerical model was calibrated against the measured infiltration rates in each subplot, the highly transient, measured seepage rates in each tray unit, and the measured travel times.

### 3.1. Governing equations

The continuum approach has generally been used for modeling unsaturated flow at Yucca Mountain (Doughty, 1999; Wu et al., 1999; Finsterle, 2000; Finsterle et al., 2003; Liu et al., 2003b). For example, the multiple interacting continua (MINC) approach has been used to accurately simulate the transient interaction of flow between the matrix and fractures (Pruess and Narasimhan, 1985; Pruess et al., 1999). Using this approach, fractures are represented by a fracture continuum, while the matrix is represented by a number of non-overlapping matrix continua, starting from the fracture–matrix interface and extending to the center of a matrix block. The thickness of a matrix gridblock decreases from the central matrix to the fracture–matrix interface, to capture the steep hydraulic gradients of transient flow along the interfaces between fractures and the matrix.

On the scale of an individual gridblock, it is assumed that unsaturated liquid flow can be described using Richards' (1931) equation. This equation can be written as follows

$$\frac{\partial \phi_f S_f}{\partial t} = \frac{\partial}{\partial x_i} \left( \frac{k_f k_{rf}}{\mu} \frac{\partial}{\partial x_i} (P_f + \rho g z) \right) + q_f \quad (1)$$

for fracture flow and

$$\frac{\partial \phi_m S_m}{\partial t} = \frac{\partial}{\partial x_i} \left( \frac{k_m k_{rm}}{\mu} \frac{\partial}{\partial x_i} (P_m + \rho g z) \right) + q_m \quad (2)$$

for matrix flow, where  $\phi$  is the porosity,  $S$  is the liquid saturation,  $k$  is the permeability,  $k_r$  is the relative permeability,  $\mu$  is the dynamic viscosity,  $P$  is the liquid-phase pressure,  $\rho$  is the fluid density,  $g$  is the gravitational acceleration,  $x_i$  is the Cartesian coordinate with  $z$  as its vertical component ( $z=x_3$ ),  $t$  is the time, subscripts  $f$  and  $m$  denote values for the fracture and matrix

continua, respectively,  $q_f$  is the fluid mass exchange rate between fractures and the rock matrix per unit volume of rocks (positive for flow from the matrix to fractures), and  $q_m$  is the total mass exchange rate into a matrix continuum from its connected continua (either the fracture continuum and a matrix continuum, or two matrix continua) per unit volume of rocks. In this study, we assumed that the air is passive with a reference pressure,  $P_{\text{air}}$ , and the liquid-phase pressure for continuum  $a$  ( $a=f, m$ ) is related to the capillary pressure,  $P_c$ :

$$P_a = P_{\text{air}} + P_{ca}. \quad (3)$$

Relative permeability and capillary pressure for continuum  $a$  ( $a=f, m$ ) are functions of liquid saturation as given by van Genuchten (1980):

$$k_{ra} = S_{ea}^{1/2} \left( 1 - (1 - S_{ea}^{1/m_a})^{m_a} \right)^2, \quad (4)$$

$$P_{ca} = -\frac{1}{\alpha_a} (S_{ea}^{-1/m_a} - 1)^{1-m_a}, \quad (5)$$

where the effective saturation  $S_e$  is defined as

$$S_{ea} = \frac{S_a - S_{ra}}{1 - S_{ra}}, \quad (6)$$

van Genuchten  $\alpha^{-1}$  is the characteristic capillary strength, and van Genuchten  $m$  is the slope parameter defining the capillary pressure and saturation curve, and  $S_r$  is the residual liquid saturation.

### 3.2. Column-based heterogeneity

To capture the spatial variabilities in infiltration and seepage rates measured in the test, we used a column-based heterogeneity method in the modeling analysis (Zhou et al., 2004). With this method, a number of rock columns can be selected for each hydrogeologic unit, based on available flow-system data (e.g., flow rates) and measured rock properties. Uniform rock properties within each rock column are assumed, whereas different rock properties may exist between different rock columns. The flow redistributes among different columns within the same hydrogeologic unit, because of lateral differences in rock properties. The introduced deterministic heterogeneity was based on the following three considerations: (1) previous fracture-network modeling has demonstrated that unsaturated flow paths within a fracture network are generally vertical, as a result of gravity-dominated flow (e.g., Liu et al., 2002); (2) the mapped fractures are near-vertical in the study area as well as around the two tunnels; and (3) rock properties for each column can be calibrated using the measured seepage rates through Niche 3 or infiltration rates through Alcove 8. A simple model of heterogeneity generally involves a relatively small number of parameters to be calibrated.

The number of rock columns within the upper (or lower) unit was determined from available data (for model calibration) on the infiltration (or seepage) series. In this test, 12 infiltration subplots with measured infiltration rates were available. As a result, there were 12 rock columns in the upper unit, each of which corresponding to an infiltration subplot. An additional rock column was used for the rock mass surrounding the central 12 columns. For the lower unit, 12 central rock columns and an additional rock column for the rock mass surrounding the central 12

rock columns were defined. Each of the central blocks corresponded to the configuration of a seepage tray unit. Tray Unit 11, the largest tray unit, was divided into three parts and regrouped into three rock columns (ranging from 10 to 12), because the same discretization in the  $x$  direction (cross Niche 3) was used in the numerical grid for a row of gridblocks in the  $y$  direction (along Niche 3) (see Fig. 8). Note that the configuration of the 12 central rock columns in the lower unit is different from that in the upper unit, because of the configuration of the infiltration subplots and the tray units of the seepage capture system (see Figs. 1 and 2).

### 3.3. Model development

A three-dimensional numerical model was employed to simulate the variably saturated flow in fractured rock using TOUGH2, a numerical simulator for non-isothermal flows of multicomponent, multiphase fluids in one, two, and three-dimensional porous and fractured media (Pruess et al., 1999).

#### 3.3.1. Three-dimensional mesh

Fig. 8 shows a three-dimensional domain used for simulations. The domain is bounded at the top by the floor of Alcove 8, and at the bottom by the floor of Niche 3, with a thickness of approximately 25 m. The niche is located in the center and represented by an open space. For simplicity, the niche ceiling is approximated by a flat surface 3.2 m above the niche floor. The domain is 20 m wide and 10 m long along the niche axis, determined from the water moisture plume observed by radial boreholes drilled around the niche. Shown at the top of the grid are the 12 infiltration subplots and the projected boundary of the niche ceiling. The domain contact between the upper and lower units is approximated by a horizontal surface, located at 14.5 m below the alcove floor (top boundary). To capture diverted water flow around the contact interface caused by difference in rock properties, fine vertical discretization of 0.2 m is

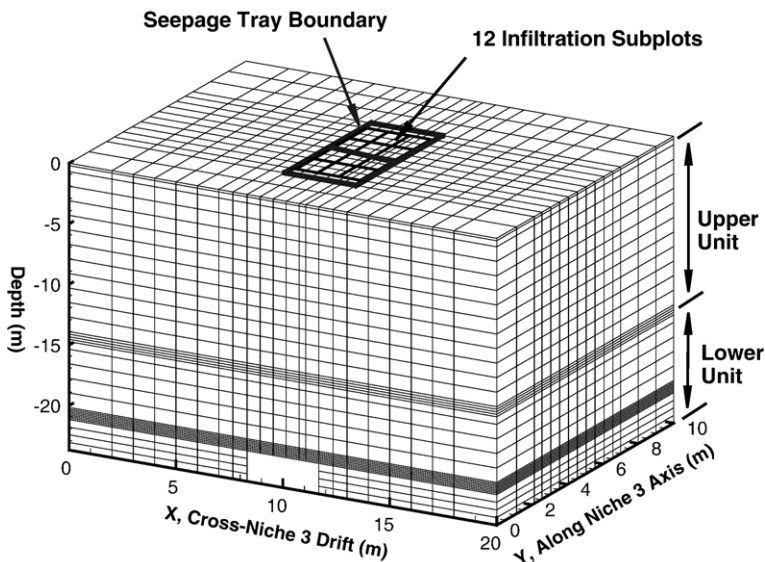


Fig. 8. Model domain and the three-dimensional grid used for the numerical model development and calibration.

used around the interface. Fine vertical discretization of 0.1 m is also used to accurately capture diverted water flow around the niche ceiling caused by capillary barrier effects (Philip, 1990; Finsterle, 2000). In the horizontal plane, a fine grid size of  $0.61\text{ m} \times 0.5\text{ m}$  is used for the central area of the infiltration and seepage test. Each infiltration subplot covers  $2 \times 2$  gridblocks, and each rock column in the lower unit covers  $1 \times 4$  gridblocks. Coarse blocks (e.g.,  $1\text{ m} \times 1\text{ m}$ ) are used for the zone away from the central area of the test. As discussed above, for each gridblock there are one fracture block and five matrix blocks, because the MINC method is used to represent the interaction between fractures and the matrix. In total, there are 67,320 blocks (for fractures and the matrix) and 140,000 connections in the three-dimensional mesh.

### 3.3.2. Boundary and initial conditions

Two possible boundary conditions could be specified at the infiltration plot, because both water head and water flux were quantified in the test. The constant water-pressure head (2 cm) might be specified at the infiltration plot. However, this condition produces relatively stable infiltration rates (over time) into the underlying system, when the time-independent saturated hydraulic conductivity is assumed. It is unrealistic to specify the constant head boundary conditions with a time varying saturated hydraulic conductivity to represent the observed transient infiltration rates. As a result, the constant-head condition was not used here. Instead, the measured infiltration rates as a function of time (reflecting the complex dynamic behavior of the time-dependent saturated hydraulic conductivity for rock immediately beneath the infiltration plot, and the capacity of flow within the water-conducting fracture network) were used as boundary conditions at the infiltration plot. The infiltration rates measured at each infiltration subplot were specified as the condition for the boundary covered by that subplot. The remaining area at the top boundary was assumed to be impervious, and the side boundaries corresponded to no-flow conditions. The ceiling and sidewall boundary of the niche was modeled by a zero-capillary-pressure condition, representing capillary barrier effects (Finsterle, 2000). The other bottom boundary was assigned free drainage conditions.

The initial water saturation in the matrix and fracture continua was difficult to ascertain, because the ambient flow conditions were disturbed by an infiltration and seepage test on the fault (see the minor fault in Fig. 2) conducted before the current test (Liu et al., 2004; Salve et al., 2004), and by construction water used for the excavation of Alcove 8. The actual matrix saturations were expected to be higher than the ambient values (i.e., 0.72 for the upper unit and 0.85 for the lower unit (Flint, 1998b)). In the model analysis, 0.86 and 0.92 were arbitrarily used as the initial matrix saturation values for the upper and lower units, respectively. A high degree of uncertainty may exist in the initial conditions used, but this uncertainty may not have a significant effect on the infiltration and seepage series at the later time of the test. A uniform fracture saturation of  $1.05 \times 10^{-2}$  (for the ambient conditions) was used for both hydrogeologic units, because fractures can drain quickly and recover from previous wetting events.

### 3.3.3. Fracture and matrix properties

The rock properties of the matrix continuum used in the model are effective porosity ( $\phi_m$ ), permeability ( $k_m$ ), van Genuchten  $\alpha$  ( $\alpha_m$ ) and van Genuchten  $m$  ( $m_m$ ). Matrix rock properties obtained from the calibration of rock properties for the site characterization of Yucca Mountain were used (BSC, 2003b), because it was believed that these matrix rock properties are relatively

homogeneous for the entire mountain. These rock properties, in the order:  $\phi_m$ ,  $k_m$ ,  $\alpha_m$ , and  $m_m$ , are  $0.15$ ,  $3.08 \times 10^{-17} \text{ m}^2$ ,  $2.13 \times 10^{-5} \text{ Pa}^{-1}$ , and  $0.30$  for the upper unit, respectively; and  $0.11$ ,  $4.07 \times 10^{-18} \text{ m}^2$ ,  $3.86 \times 10^{-5} \text{ Pa}^{-1}$ , and  $0.29$  for the lower unit, respectively. Fracture  $m$  ( $m_f$ ) value of  $0.61$  for site characterization was used for both the upper and lower units. In addition to these mountain-scale rock properties, all other fracture properties specific to the test site were used, because of the strong spatial variability in these rock properties. These fracture properties included fracture porosity ( $\phi_f$ ), fracture permeability ( $k_f$ ), fracture van Genuchten  $\alpha$  ( $\alpha_f$ ), and fracture frequency (or density). Fracture frequency of  $1.0$  and  $1.5 \text{ m}^{-1}$  was used to define the interface area between fractures and the matrix per unit volume of rock mass for the upper and lower units, respectively (see Section 2.1). The fracture porosity of  $6.6\%$  and  $1.0\%$  calibrated from a nearby fault test (Liu et al., 2004) was used for the upper and lower units, respectively. The calibration of the remaining two rock properties ( $k_f$  and  $\alpha_f$ ) at the test site is described in the following section.

### 3.4. Model calibration

The flow model developed in Section 3.3 was calibrated to match temporal and spatial variabilities in measured infiltration and seepage rates. Through this calibration, site-specific rock properties (and column-specific rock properties for heterogeneity) were obtained. The rock parameters to be calibrated were  $k_f$  and  $\alpha_f$  for each of the 13 rock columns in the lower unit,  $k_f$  for each of the 13 rock columns in the upper unit, and  $\alpha_f$  assumed to be common for the central 12 columns and for the rest of the rock mass column in the upper unit. This assumption was based on the fact that the infiltration rate for a rock column is not sensitive to the  $\alpha_f$  value in the rock column. There were a total of 41 unknowns to be calibrated, 26 parameters for the lower unit and 15 parameters for the upper unit.

The calibration proceeded in stages guided by available information and physical consideration. For the upper unit, the infiltration data in 12 subplots were used to better constrain the  $k_f$  unknowns. For each rock column, an initial  $k_f$  value was determined by matching the maximum measured infiltration rate (excluding the first day) and the simulated infiltration rate. The maximum infiltration rate was considered to be the saturated hydraulic conductivity for the column (Faybishenko et al., 2003). The top flow boundary condition in the case of determining initial  $k_f$  values was the  $2 \text{ cm}$  water head constant with time. A trial-and-error method was used to reduce the mismatch between the measured maximum infiltration rate and the stable infiltration rate for a given  $k_f$  value. (Note that the boundary conditions of a water head of  $2 \text{ cm}$  used for determining the initial  $k_f$  values are different than those of infiltration rates used for the model calibration.) The fracture permeability obtained for each rock column was further calibrated using a scale factor. The final calibrated  $\log k_f$  for a rock column was the product of the calibrated scale factor and the  $\log k_f$  obtained by the trial-and-error method. In this way, the effects of observed spatial variability in infiltration rates were generally captured by model calibration, and the number of unknowns to be calibrated reduced to 30. In the following model calibration, the measured time-dependent infiltration rates were used as the top boundary condition.

The data used for the calibration (primarily for the lower unit) included the series of measured seepage rates for each of the 12 tray units and the travel time of 29 days measured at a location  $0.5 \text{ m}$  above the niche ceiling. Because of strong temporal variability in the measured seepage rates, the entire seepage series was divided into three time periods: (1) the first 30 days with no or little seepage, (2) the next 60 days with strongly (temporarily) varying seepage rates, and (3) the



last 125 days with quasi-stable seepage rates. The objective function in the model calibration was defined by:

$$\text{obj.} = \sum_{j=1}^{13} \left( \sum_{t=1}^{30} \omega_1 (q_{jt}^o - q_{jt}^s) + \sum_{t=31}^{90} \omega_2 (q_{jt}^o - q_{jt}^s) + \sum_{t=91}^{215} \omega_3 (q_{jt}^o - q_{jt}^s) + \sum_{t=1}^{20} \omega_4 (0 - q_{jt}^s) \right), \quad (7)$$

where  $q_{jt}$  is the seepage rate at the  $t$  day (from liquid release) for the  $j$  tray unit ( $j=13$  for the total seepage rate), superscripts  $o$  and  $s$  denote observed and simulated values, respectively, and  $\omega$  is the weight factor. The first three terms in Eq. (7) represent the misfit between measured and simulated seepage rates, and the last term represents the misfits between measured and simulated travel times. Different values for the weight factor were used for different time periods because the seepage exhibited varying dynamic behavior from one time period to another. For the first term, no or little seepage occurred and a small weight was used; for the second term, the strong temporal variability of seepage rates is an important indicator of the unsaturated system, and the same weight ( $\omega_2 = \omega_1$ ) was used; a value of  $\omega_3 (=2\omega_1)$  was used to focus on the later, quasi-stable seepage rates because the quasi-stable flow condition was to be used for tracer tests. Because it was difficult to introduce the misfit between the simulated and measured travel times of wetting fronts, we used the misfit between the measured and the simulated seepage rates to constrain misfits of the travel times. A higher weight factor ( $\omega_4 = 5\omega_3$ ) was used in the last term of Eq. (7) to force seepage not to occur within the first 20 days, while allowing for the occurrence of seepage between the 21st and 30th day, because the smaller weight factor ( $\omega_1$ ) was used for this period. The reason for doing this was that many factors (e.g., dynamic connectivity of water-conducting fractures) affecting the wetting-front travel times could not be captured in the current continuum-based numerical model. Note that the available data on the travel times in this test can help significantly reduce the uncertainties in the estimates of advection (or mean residence time) from a field tracer test in fractured rock (Liu et al., 2004; Zhou et al., 2006).

The model calibration reduced the objective function by adjusting the 30 unknown parameters for rock properties. Calibration was performed using the inverse modeling code iTOUGH2 (Finsterle, 1999). The parallel version of iTOUGH2 was used to reduce calibration time, because each forward run for variably saturated flow with strong transient behavior was computational-time consuming. The calibration time needed for the parallel calibration was a small fraction (approximately 10%) of that needed for nonparallel calibration, making it possible to calibrate the spatial variability of rock properties in such a complex unsaturated flow system.

#### 4. Results and discussion

The calibrated seepage rates for the 12 central rock columns of the lower unit and for total seepage rates were compared to their corresponding measured values as functions of time. We were interested in exploring whether the current numerical model was able to represent the spatial variabilities in measured infiltration and seepage rates, and to capture their temporal variabilities resulting from the dynamic behavior of water-conducting fractures. Calibrated fracture properties in the upper and lower units were also given in terms of their deterministic spatial variabilities. We were also interested in exploring the relationship between the mapped discrete fractures and the calibrated rock properties (or the

measured infiltration/seepage rates) to investigate to what degree the latter can be inferred from fracture maps alone.

#### 4.1. Calibration results

##### 4.1.1. Calibrated seepage rates

Fig. 9 shows the match between the measured total seepage rate for the entire niche and the simulated total seepage rate using calibrated rock properties. The match is good for the entire test period, in particular for the later time. The very good match at a later time may result from the high weight factor used for the later-time seepage rates in the objective function of Eq. (7). The quasi-stable nature of seepage and infiltration rates at later time also helps produce good matches. During the early time between the 30th and 90th day, the match is also reasonable. The simulated maximum seepage rate is close to the measured one.

The simulated seepage occurs on the 20th day, earlier than the measured seepage, which occurs on the 29th day after liquid release. The difference in the wetting-front travel times can be explained by the handling of different kinds of data in the objective function of Eq. (7). In model calibration, a large weight factor ( $\omega_1 + \omega_4$ ) was used to practically force seepage not to occur within the first 20 days, while a smaller weight factor ( $\omega_1$ ) was used for the misfit between the measured and calibrated seepage rates between the 21st and 30th day, allowing for the occurrence of seepage during this period. The measured wetting-front travel times are affected by many factors (e.g., initial water storage in cavities neglected in the effective fracture porosity used and dynamic connectivity of water-conducting fractures) active in the early time of the test. Such factors could not be considered in the current continuum-based numerical model. If a period of 29 days for no-seepage occurrence was used, the calibrated fracture permeability would be too small to be reasonable for the test site.

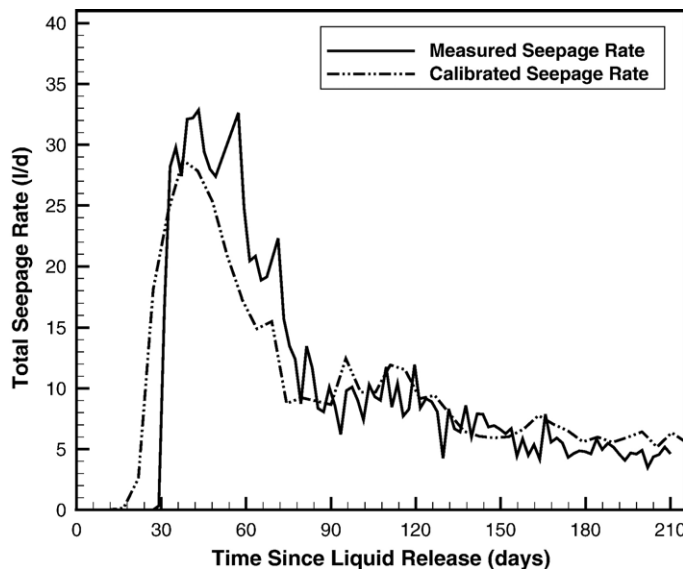


Fig. 9. Match between measured (transient) total seepage rates and simulated rates using calibrated rock properties.

Fig. 10 shows the match between calibrated and measured seepage series associated with the 12 rock columns in the lower unit. The match is generally good in terms of the time-dependent behavior. Simulated and measured seepage rates for Column 12 are close to each other. For Column 7, however, significant differences between simulated and measured seepage rates are obtained between the 30th and 90th day, but a good match is obtained for the later time, with low seepage rates. Again, this may result from the high weight factor used for the misfit of later-time seepage rates, and the stronger dynamic effects in the measured seepage rates at early time. For some columns, measured seepage rates decline with time faster than simulated ones at later time, possibly because of the many dynamic effects of fragmented unsaturated flow in fractured rock.

The good match for the total seepage rates indicates that the continuum approach used is able to simulate complex unsaturated flow in the mesoscale test system, in which smaller-scale variabilities in the dynamic behavior of seepage are averaged out. The reasonable match for seepage rates for each of the 12 tray units also demonstrates that the calibrated heterogeneity in fracture permeability and fracture capillary strength (corresponding to  $\alpha_f^{-1}$ ) can be used to reproduce the spatial variability in the measured seepage rates. Measured infiltration and seepage rates are indicative of the lumped effects of complicated fracture connectivity, flow interaction between fractures and matrix, and active fractures and fracture segments. The calibrated rock properties reflect the lumped effects of various factors on unsaturated flow, and are representative

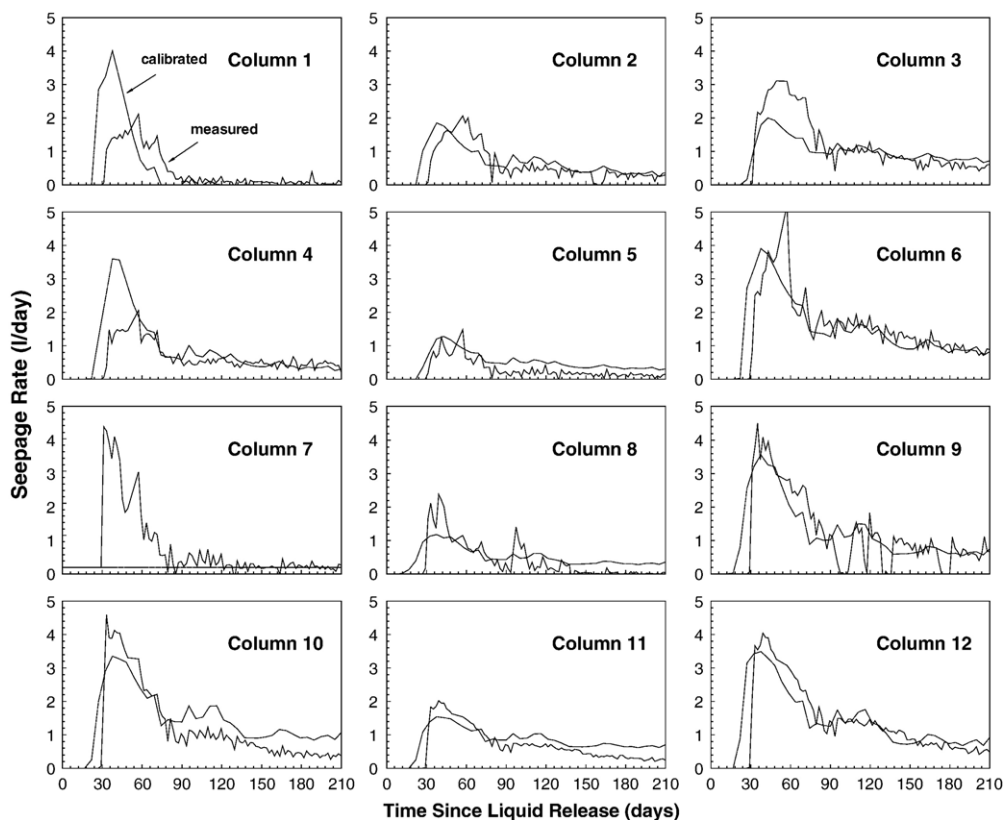


Fig. 10. Matches between measured seepage rates (solid lines) and simulated seepage rates (dash-dot-dot lines) using calibrated rock properties for the 12 seepage rock columns.

of actively participating fractures in the fracture network and active segments within individual fractures.

#### 4.1.2. Calibrated rock properties

Fig. 11 shows the calibrated  $k_f$  and  $\alpha_f$  values for the 13 rock columns in the upper and lower units. The calibrated  $k_f$  values for the 12 central rock columns in the upper unit reflect the spatial variability in the measured infiltration rates over the infiltration plot, because the maximum measured infiltration rates were used for constraining the  $k_f$  calibration. The largest  $k_f$  of  $1.86 \times 10^{-13} \text{ m}^2$  is located in Rock Column 11 (corresponding to Subplot 11), where the maximum measured infiltration rate is 119.7 l/day (see Fig. 4). The smallest  $k_f$  of  $1.31 \times 10^{-14} \text{ m}^2$  is situated in Column 7. The maximum measured infiltration rate for Column 7 is 7.0 l/day, which is 17 times less than that in Subplot 11. The calibrated  $k_f$  varies over one order of magnitude in the 12 central rock columns. This spatial variability is within the range of air permeability values measured in 0.3 m intervals of six 15 m long near-vertical boreholes drilled around the infiltration plot. The measured air permeability varies over five orders of magnitude, ranging from  $3.60 \times 10^{-15}$  to  $6.25 \times 10^{-9} \text{ m}^2$  (BSC, 2003a). The geometric mean of the calibrated  $k_f$  values for the 13 rock columns is  $4.90 \times 10^{-14} \text{ m}^2$ , slightly lower than that of the measured air permeability ( $7.94 \times 10^{-14} \text{ m}^2$ ). The standard deviation of calibrated  $\log k_f$  (0.37) is smaller than that (1.29) for the measured air permeability, indicating that the spatial variability of permeability decreases with increase in the sampling size (the size for rock columns is much larger than the 0.3 m intervals

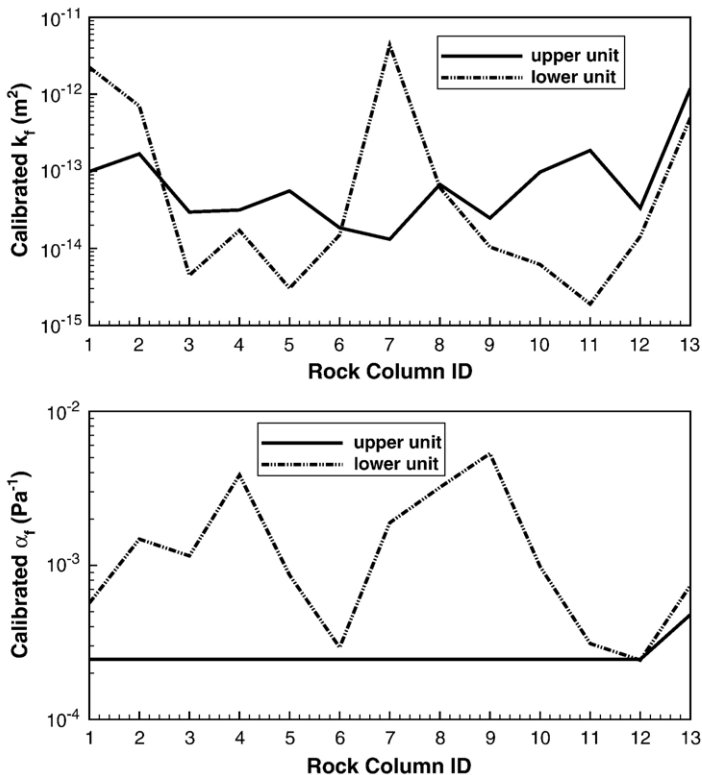


Fig. 11. Calibrated fracture permeability and van Genuchten  $\alpha_f$  for the upper and lower hydrogeologic units.

used for measuring air permeability). This is consistent with the theoretic findings on scale-dependent permeability (Neuman, 1994).

Calibrated  $k_f$  for Column 13 (for the rock mass surrounding the central rock columns) is  $1.20 \times 10^{-12} \text{ m}^2$ , one order of magnitude larger than the largest  $k_f$  in the central rock columns. Such a difference in the calibrated  $k_f$  may result from the inability of the current numerical model to capture flow diversion caused by nonvertical fractures. In such nonvertical fractures, water flows within fracture planes until fracture intersections are encountered. This kind of water-diversion mechanism can be handled in the current continuum-based model only by using the strong heterogeneity of rock properties in the lateral direction. The large  $k_f$  calibrated for Column 13 facilitates the lateral water flow from the central columns.

The calibrated  $k_f$  values for the lower unit vary over three orders of magnitude for the 13 rock columns, ranging from  $1.89 \times 10^{-15}$  to  $4.34 \times 10^{-12} \text{ m}^2$ . Large calibrated  $k_f$  values occur at Columns 1, 2, 7, and 8, where the seepage rates through their corresponding tray units are relatively low. For example, the calibrated  $k_f$  for Column 1 is  $2.25 \times 10^{-12} \text{ m}^2$  (the second largest), while the seepage rate at early and later times is the lowest. Lower calibrated  $k_f$  values occur for rock columns with higher seepage rates at both early and later times. For example, the calibrated  $k_f$  for Column 12 is  $1.43 \times 10^{-14} \text{ m}^2$ , but its seepage rate is the second highest at both early and later times. The range of calibrated  $k_f$  values is similar to that of the measured air permeability, which ranges from  $1.43 \times 10^{-15}$  to  $6.22 \times 10^{-12} \text{ m}^2$ . The mean calibrated  $\log k_f$  is  $-13.38$ , which is close to that of  $\log$  air permeability ( $-13.40$ ).

The calibrated  $\alpha_f$  (in  $\text{Pa}^{-1}$ ) values for the lower unit vary over 1.5 orders of magnitude in space, with  $\log \alpha_f$  ranging from  $-3.62$  to  $-2.27$ . The mean and standard deviation are  $\log \alpha_f = -2.97 \pm 0.45$ . The spatial variability in the calibrated  $\alpha_f$  corresponds well with that of the normalized seepage rate (see Fig. 7). In the  $x$  direction (see Fig. 8), the relative  $\alpha_f$  values over several rock columns can be interpreted by the magnitude of normalized seepage rates. For example, the calibrated  $\alpha_f$  values for Columns 3–6 in the first tray unit row demonstrate that a smaller  $\alpha_f$  value (higher capillary strength) corresponds to a higher seepage rate. The measured seepage rate in Tray Unit 6 is the highest among the four columns, and the calibrated  $\alpha_f$  for Column 6 is the lowest. The same situation is true for Columns 9–12 (Columns 11 and 12 share the same normalized seepage rates in Tray Unit 11). The lowest  $\alpha_f$  value is obtained for Column 12, where the highest seepage rate is measured in the second row of tray units.

The calibrated rock properties may not be unique, because 30 rock properties were calibrated simultaneously. However, the pair of rock properties for a column in the lower hydrogeologic unit corresponded to a unique seepage dataset, thus significantly reducing the calibration uncertainties. This can be seen from the relatively strong correlation between the calibrated  $\log k_f$  and the mean later-time seepage rates, with a correlation coefficient of  $-0.70$  (as well as for the calibrated  $\log \alpha_f$  values). In addition, the calibrated  $\log k_f$  and  $\log \alpha_f$  values are not correlated, because a weaker correlation between  $k_f$  and  $\alpha_f$  in fracture networks than in porous media is expected and the capillary strength in fracture networks is much smaller than in porous media (Zhou et al., 2002). This lack of correlation also helps reduce calibration uncertainties.

#### 4.2. Discussion

So far, model development and results are presented within the framework of the continuum approach and deterministic column-based heterogeneity, without any indication of the discrete fractures shown in Figs. 1 and 2. In this section, we will discuss (1) the roles that discrete fractures play in the measured infiltration and seepage rates, (2) the relationship between the fracture

geometric characteristics (i.e., fracture density) and the calibrated rock properties, and (3) to what degree the measured infiltration and seepage rates and the calibrated rock properties can be inferred by the mapped fracture patterns at the top and bottom boundaries.

#### 4.2.1. Discussion on the transient infiltration rates

Before the analysis on spatial variabilities of measured infiltration and seepage rates and of calibrated rock properties in the following sections, we would like to discuss the transient features of infiltration and seepage rates observed in the test. As shown in Figs. 3 and 4, the total infiltration rate and the infiltration rate for a number of infiltration subplots (e.g., Subplots 1, 2, 10, and 11) exhibit strong temporal variability. The reduction in infiltration rates (over time) may primarily result from the failure of water-conducting fractures (and active portions of fractures) to transmit water (Faybishenko et al., 2003). The internal fracture connectivity is complicated: some fractures may not connect with other fractures, while others are connected to each other; only a fraction of all fractures are globally connected. The fracture connectivity (which affects infiltration) is also related to the scale of water percolation. Infiltrated water through the infiltration plot flows downward along fractures. Once the dead ends of fractures are reached, the infiltrated water fills in the dead-end fractures, and these fractures no longer contribute to infiltration. We refer to this situation as a failure of the fractures in conducting infiltrated water. The failure of water-conducting fractures is time-dependent. As the infiltration process proceeds, fractures initially conducting water may no longer conduct water (because they are not globally connected), leading to fewer fractures conducting water flow and a decrease in infiltration rates. Meanwhile, the infiltrated water moves downward, and fracture connectivity becomes more important to unsaturated flow and to the infiltration process. The fracture-failure mechanism affects the transient infiltration rates, but it may not participate in the quasi-steady-state flow regime at later time. At later steady-state time, the infiltrated water flows through active, globally connected fractures, and the infiltration rates tend to be stable. Note that the above discussion focuses on the infiltration rates since the 30th day, because the complex transient nature within the first 30 days of the test was affected by many other factors, such as dynamic movement of in-fill materials, and discharge and dissolution of entrapped air. The above interpretation is consistent with the findings obtained by a numerical model for a field infiltration test in Idaho (Doughty, 2000). In Doughty's model, the tributary structure of a fracture pattern was explicitly considered within the matrix block. Doughty's model reproduced the general trend of decreasing infiltration rate, which was representative of a funneling of flow (Faybishenko et al., 2000).

The transient failure of water-conducting fractures (and active portions of fractures) could not be captured by the current continuum-based numerical model through the structure of discrete fracture network. However, these fractures' effects on the (transient) seepage responses were captured using the transient infiltration rates as the top boundary conditions.

#### 4.2.2. Fracture density and measured infiltration rate

Fig. 12 shows the positive correlation between normalized infiltration rates and fracture density. The fracture density for an infiltration subplot is calculated using total fracture trace length surveyed over the surface area of the subplot. A number of fractures intersect the infiltration plot, allowing for infiltration through the fractures (see Fig. 1). The fracture density varies from zero to  $4.03 \text{ m}^{-1}$  (in Subplot 11), with an average value of  $1.31 \text{ m}^{-1}$  (over 12 subplots). Four different cases for the relationship between measured infiltration rates and fracture density are evaluated for the 12 subplots.



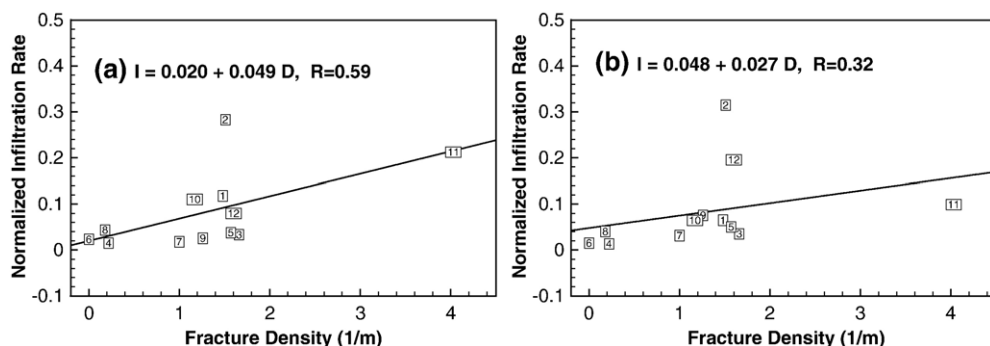


Fig. 12. Correlation between the normalized infiltration rates ( $I$ ) measured during (a) the first highly transient 90 days and (b) the later quasi-steady-state 125 days, and fracture density ( $D$ ) calculated for each infiltration subplot at the floor of Alcove 8. Note that  $R$  is the correlation coefficient.

In the first case, generally low infiltration (for Subplots 4, 6, and 8) occurs because no fractures longer than 1.0 m are involved (with zero fracture density) or only a very short segment of a large fracture is involved (with a very small fracture density). The low infiltration occurs through small fractures, which are not included in the fracture map. Infiltration rates are relatively stable after the first-day high infiltration, which may have resulted from the large water-storage capacity of small fractures and cavities and the imbibition of unsaturated matrix in the rock beneath the subplots.

In the second case, the measured infiltration rate is relatively low and stable with time, although one or two large fractures intersect Subplots 3, 5 and 7, leading to a fracture density close to its mean value. The infiltration series in these subplots, similar to those in the first case, imply that not all mapped fractures (or fracture segments) within these subplots are globally connected, or actively conduct water flow.

In the third case, the relatively high infiltration rates measured in Subplots 1, 2, 10, and 11 may stem from generally large fracture density and fracture intersections in these subplots. For example, four fractures intersect Subplot 11, leading to the highest fracture density. One or two large fractures pass through the other three subplots (Subplots 1, 2, and 10), leading to fracture density close to its mean value. However, these fractures extend out of the infiltration plot, which may allow for in-fracture-plane flow diversion into areas out of the infiltration plot (Dahan et al., 1999). Also note that fractures intersect each other within these infiltration subplots, and infiltrated water can move through the connected fractures, possibly enhancing infiltration. The four subplots also share a similar three-stage pattern for infiltration rates, which is similar to that of the total infiltration rate (see Fig. 4). The infiltration rate in Subplot 2 is high at both early and later times, because the infiltrated water may flow within a well-connected fracture network. For Subplots 1, 10, and 11, the infiltration rate is high at early time but relatively low at later time, possibly because some water-conducting fractures active at early time may fail in conducting water at later time (Doughty, 2000; Faybishenko et al., 2003).

In the final case, substantial and stable infiltration occurs in Subplots 9 and 12, possibly because of the relatively large fracture density and a well-connected fracture network. Large fractures intersect these subplots and extend out of the infiltration plot area. Fracture mapping also indicates that there are a very large number of small fractures (not included in the fracture map) around the two subplots. These large and small fractures may enhance fracture connectivity in the fractured rock under these two subplots. This enhanced connectivity produces stable infiltration rates over the entire test period, with little dynamic behavior.

The positive, but not strong, correlation between normalized infiltration rates and fracture density represents the effects of preferential flow caused by heterogeneity in single fracture planes and fracture networks. The heterogeneity may stem from (1) the spatially varying distributions of hydraulic apertures, (2) the connectivity of fractures underlying the infiltration plot, and (3) conditions of in-fill materials within fractures (Wealthall et al., 2001). For example, for the single fracture passing through Subplots 2, 5, and 9, the infiltration rates for the fracture segments within these three subplots are very different, indicating flow focusing in small segments of the fracture. The spatial variability of infiltration rates along single fractures indicates that the in-plane heterogeneity plays a critical role in controlling water percolation. This is consistent with the findings observed by Dahan et al. (1999) in a single fracture, through which only 50% of the open fracture segments allowed significant flow, and less than 20% of the fracture opening transmitted high flow rates. The in-fracture-plane and fracture-network heterogeneity produces preferential flow in the saturated rock immediately underlying the infiltration plot and in the underlying unsaturated zone. As a result of the preferential flow, the correlation between infiltration rates and fracture density becomes smaller, but the infiltration rates are still correlated, to a certain degree, to the fracture density on the infiltration plot.

The correlation between normalized infiltration rates and fracture density varies from the high infiltration of early time to the low infiltration of later time, as shown in Fig. 12. The correlation for the early time (with a correlation coefficient of 0.59) is stronger than that for the later time (with 0.32). The different correlations may result from the different dynamic behavior of infiltration rates in different subplots (see Fig. 4). The infiltration rates remain stable during both time periods in a number of subplots (i.e., Subplots 2–8), whereas significant change in the infiltration rates is observed from early to later time for the other subplots (i.e., Subplots 1 and 9–12). More importantly, the different correlation results from the transient nature of total infiltration rates. A smaller total infiltration rate at later time produces more fragmented unsaturated flow in the underlying fractured rock, with less pervasive patterns of viscous-force-dominated flow in the upper portion of the underlying fractured rock than the early high-infiltration time. Because of the different flow features, a smaller infiltration rate results in smaller correlation between fracture density and infiltration rates.

In summary, the positive correlation between measured infiltration rates and fracture density indicates that discrete fractures in the infiltration plot play a critical role in water percolation, especially in the early-time flow regime. The measured infiltration rates reflect the effects from the total actively water-conducting fractures (and fracture segments), while the fracture density calculated using the fracture map on the alcove floor does not distinguish active fractures (segments) from inactive ones. In addition, in-fracture-plane heterogeneity and complicated dynamic effects also affect such correlations, indicating that capturing the discrete features of a fracture network does not mean fully capturing the complicated unsaturated flow.

#### 4.2.3. Fracture density and calibrated permeability of the upper unit

Fig. 13 shows a positive correlation between calibrated  $\log k_f$  of the upper unit and fracture density. This correlation demonstrates that the calibrated fracture permeability partially captures the spatially varying discrete fractures within the infiltration plot. The largest calibrated fracture permeability in Rock Column 11 corresponds to the highest calculated fracture density in Subplot 11. However, the correlation is not very strong, with a correlation coefficient of 0.55. This positive but not strong correlation indicates the importance of flow focusing resulting from in-fracture-plane heterogeneity in single fractures (Dahan et al., 1999; Salve et al., 2004), and of the connectivity of actively water-conducting fractures in fracture networks (Liu et al., 1998; Glass et

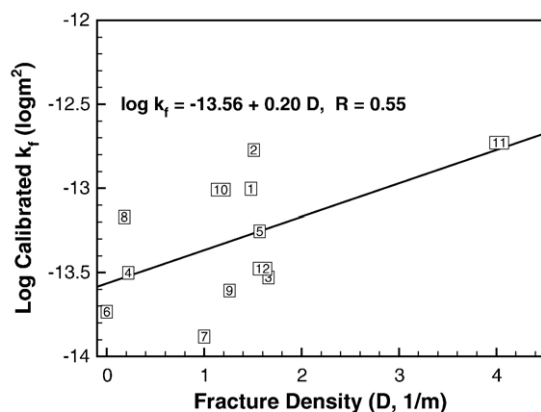


Fig. 13. Correlation between calibrated fracture permeability ( $m^2$ ) of the upper hydrogeologic unit and fracture density ( $m^{-1}$ ) mapped on the alcove floor.

al., 2002; Liu et al., 2003a). The calibrated fracture permeability also includes contributions from small fractures, because non-zero infiltration rates were observed for subplots with zero fracture density (without considering small fractures). The calibrated fracture permeability is believed to represent the actively participating fractures (or fracture segments), which are reflected in the measured infiltration rates.

#### 4.2.4. Fracture density and measured seepage rates

Unlike the positive correlation between fracture density and measured infiltration rates, no correlation was found between the early-time seepage rates and fracture density, and a weakly negative correlation was found for the later-time seepage rates. (The fracture density was calculated for each tray unit using natural fractures on the fracture map shown in Fig. 2. The fracture density was obtained by dividing the total fracture trace length surveyed by the surface area of the tray unit.) This lack of correlation can be attributed to the complicated unsaturated flow in the fracture network and flow diversion in the vicinity of Niche 3.

Flow in the fracture network transits from saturated flow in the upper portion of the system to complex unsaturated flow under conditions of low percolation rates in the lower portion of the system, particularly in the vicinity of the niche. The unsaturated flow in the lower portion of the system is complicated by many factors. First, seepage drips into the niche through fractures, because of dominant fracture flow and little matrix flow in the lower unit. Second, in-fracture-plane heterogeneity leads to fragmented and fingered flow within single fractures. Such a flow is not a function of fracture trace length represented by fracture density. Flow fragmentation and fingers are major features of unsaturated flow in fractured rock under low-flow-rate conditions (Glass et al., 2002). Finally, the mapped fractures on the niche ceiling may be globally connected, but the global unsaturated flow occurs only in a fraction of the connected fractures, as represented by the active fracture model (Liu et al., 1998). The lack of correlation demonstrates the importance of fragmented and fingering flow within single fractures, and of active fractures in a fracture network.

The lack of correlation between normalized seepage rate and calculated fracture density also demonstrates the importance of water diversion around the niche caused by (1) small fractures

and excavation-induced fractures, (2) capillary-barrier-layer effects, and (3) film flow on the niche ceiling. First, small fractures and excavation-induced fractures may be connected with water-conducting fractures above the niche. For example, water in a water-conducting fracture, which ends at a distance above the ceiling, may be redistributed (or diverged) into such connected small fractures, and may disperse on the niche ceiling. In addition, small fractures can imbibe water at fracture intersections from large fractures, because the small fractures have higher capillarity than the large fractures. The excavation of the niche induced many fractures around the niche ceiling, enhancing fracture connectivity in different directions and facilitating flow diversion. Secondly, capillarity is a very important mechanism for water diversion around the niche ceiling (Philip, 1990; Finsterle, 2000). A capillary barrier layer exists above the niche ceiling, because of the zero-capillarity boundary condition on the ceiling and sidewall of Niche 3. Within the capillary barrier layer, flow can redistribute among all connected fractures, leading to weaker correlation between the normalized seepage rate and the calculated density of large fractures. Finally, water flow leaving from fractures may flow around the niche ceiling in the form of film flow (Tokunaga and Wan, 1997). The film flow is caused by surface roughness and the geometric shape of the niche ceiling. This type of flow was observed in seepage tests in other niches at Yucca Mountain by Trautz and Wang (2002).

## 5. Summary and conclusions

A mesoscale infiltration and water seepage test was conducted for investigating unsaturated flow in deep, fractured rock, focusing on the spatial variabilities in highly transient hydrologic responses (i.e., infiltration and seepage rates) (Salve, 2005). A methodology was developed for analyzing this field test, including (1) use of a three-dimensional unsaturated flow model, based on the multiple interacting continua (MINC) approach, to simulate the highly transient unsaturated flow in fractured rock, (2) development of the conceptual model of deterministic, column-based heterogeneity to represent the rock-property spatial variabilities reflected by variabilities of hydrologic responses, and (3) analysis of correlations between measured infiltration and seepage rates (as well as calibrated rock properties) and density of fractures mapped at the top and bottom of the test bed. The fracture permeability and van Genuchten  $\alpha_f$  were calibrated for each rock column, which corresponded to the configuration of seepage collection tray units in the lower hydrogeologic unit or the infiltration subplots in the upper hydrogeologic unit.

The calibrated numerical model is able to reproduce the highly transient, spatially varying seepage rates measured. Significant water diversion caused by fracture orientations in the discrete fracture network can be captured by the strong heterogeneity of capillary force strength and of fracture permeability in the lateral direction. The calibrated rock properties in both the upper and lower hydrogeologic units correlate well with the measured infiltration and seepage rates, which reflect lumped features of small-scale flow processes.

The positive correlation between measured infiltration rates and fracture density at the top boundary indicates that infiltration under ponded conditions is partially controlled by discrete fractures on the infiltration plot, although other factors (e.g., in-fracture-plane heterogeneity and dynamic connectivity of water-conducting fractures) also play an important role in complicating infiltration processes. The lack of correlation between measured seepage rates and fracture density on the niche ceiling indicates the importance of preferential flow paths along active, water-conducting fractures (and their active portions), and of water diversion around the niche ceiling caused by a combination of capillary barrier and possibly film flow. As a result,

continuum-based modeling of unsaturated flow in fractured rock at mesoscale or a larger scale is not necessarily conditional on discrete fracture patterns, because of strong preferential flow paths along active, water-conducting fractures.

Note that the rock properties calibrated using the field test data are effective, model-related, and process- and case-specific parameters. Although a good comparison between the calibrated fracture permeability and measured air permeability in terms of mean and variance values has been achieved, the model should be re-calibrated when used for any other sites or any other scales of investigation. The flow field at the Yucca Mountain site differs from that at the test site; therefore the results with respect to radionuclide and attenuation are not quantitatively applicable to that site. Nevertheless, the continuum-based model with deterministic heterogeneity can be considered as an efficient alternative to discrete fracture network models with stochastic rock properties.

## Acknowledgments

The authors wish to thank Eduard Hoehn at Swiss Federal Institute for Water Science and Technology, Emil Find, the Editor-in-Chief, and two anonymous reviewers for their constructive comments and suggestions, which help improve significantly the quality of the manuscript. We also thank Paul Cook, Stefan Finsterle, Dan Hawkes, and Diana Swantek for their internal technical reviews, editorial comments, or graphics support. Thanks are also due to Stefan Finsterle for his help in using the parallel version of iTOUGH2. This work has been supported by the Director, Office of Civilian Radioactive Waste Management, U.S. Department of Energy, through Memorandum Purchase Order EA9013MC5X between Bechtel SAIC Company, LLC and the Ernest Orlando Lawrence Berkeley National Laboratory (Berkeley Lab). The support is provided to Berkeley Lab through the U.S. Department of Energy Contract No. DE-AC03-76SF00098.

## References

- Barenblatt, G.E., Zheltov, I.P., Kochina, I.N., 1960. Basic concepts in the theory of homogeneous liquids in fissured rocks. *J. Appl. Math.* 24 (5), 1286–1303.
- Bear, J., Tsang, C.-F., de Marsily, G. (Eds.), 1993. *Flow and Contaminant Transport in Fractured Rock*. Academic Press, Inc., San Diego.
- Bodvarsson, G.S., Tsang, Y. (Eds.), 1999. Yucca Mountain Project. *J. Contam. Hydrol.*, vol. 38, pp. 1–146.
- Bodvarsson, G.S., Ho, C.K., Robinson, B.A. (Eds.), 2003. Yucca Mountain Project. *J. Contam. Hydrol.*, vol. 62–63, p. 750.
- Brown, S., Caprihan, A., Hardy, R., 1998. Experimental observation of fluid flow channels in a single fracture. *J. Geophys. Res.* 103, 5125–5132.
- BSC (Bechtel SAIC Company), 2003a. In Situ Field Testing of Processes. ANL-NBS-HS-000005 REV02B. Bechtel SAIC Company, Las Vegas, Nevada.
- BSC, 2003b. Calibrated Properties Model. MDL-NBS-HS-000003 REV 01. Bechtel SAIC Company, Las Vegas, Nevada.
- BSC, 2003c. Analysis of hydrologic properties data. MDL-NBS-HS-000014 REV 00. Bechtel SAIC Company, Las Vegas, Nevada.
- Cacas, M.C., Ledoux, E., de Marsily, G., Barbreau, A., Calmels, P., Gaillard, B., Margritta, R., 1990. Modeling fracture flow with a stochastic discrete fracture network: calibration and validation, 2, the transport model. *Water Resour. Res.* 26, 491–500.
- Cook, P., 2000. In situ pneumatic testing at Yucca Mountain. *Int. J. Rock Mech. Min. Sci.* 37, 357–367.
- Dahan, O., Nativ, R., Adar, E.M., Berkowitz, B., Ronen, Z., 1999. Field observation of flow in a fracture intersecting unsaturated chalk. *Water Resour. Res.* 35 (11), 3315–3326.
- Doughty, C., 1999. Investigation of conceptual and numerical approaches for evaluating moisture, gas, chemical, and heat transport in fractured unsaturated rock. *J. Contam. Hydrol.* 38, 69–106.

- Doughty, C., 2000. Numerical model of water flow in a fractured basalt vadose zone: box Canyon site Idaho. *Water Resour. Res.* 36 (12), 3521–3534.
- Doughty, C., Salve, R., Wang, J.S.Y., 2002. Liquid-release tests in unsaturated fractured welded tuffs: II. Numerical modeling. *J. Hydrol.* 256, 80–105.
- Dverstorp, B., Andersson, J., Nordqvist, W., 1992. Discrete fracture network interpretation of field tracer migration in sparsely fractured rock. *Water Resour. Res.* 28 (9), 2327–2343.
- Fabryka-Martin, J.T., Dixon, P.R., Levy, S.S., Liu, B., Brenner, D.L., Wolfsberg, L.E., Turin, H.J., Sharma, P., 1996. Implications of environmental isotopes for flow and transport in the unsaturated zone at Yucca Mountain, Nevada. *Geol. Soc. Am. Abstr. Programs* 28 (7), A-414.
- Faybishenko, B., Doughty, C., Steiger, M., Long, J.C.S., Wood, T.R., Jacobsen, J.S., Lore, J., Zawislanski, P.T., 2000. Conceptual model of the geometry and physics of water flow in a fractured basalt vadose zone. *Water Resour. Res.* 36 (12), 3499–3520.
- Faybishenko, B., Bodvarsson, G.S., Salve, R., 2003. On the physics of unstable infiltration, seepage, and gravity drainage in partially saturated tuffs. *J. Contam. Hydrol.* 62–63, 63–87.
- Finsterle, S., 1999. iTOUGH2 User's Guide. Report LBNL-40040, UC-400. Lawrence Berkeley National Laboratory, Berkeley, CA.
- Finsterle, S., 2000. Using the continuum approach to model unsaturated flow in fractured rock. *Water Resour. Res.* 36 (8), 2055–2066.
- Finsterle, S., Ahlers, C.F., Trautz, R.C., Cook, P.J., 2003. Inverse and predictive modeling of seepage into underground openings. *J. Contam. Hydrol.* 62–63, 89–109.
- Flint, L.E., 1998a. Matrix Properties of Hydrogeologic Units at Yucca Mountain, Nevada. U.S. Geological Survey Open-File Report, MOL.19970324.0046. U.S. Geological Survey, Denver, CO.
- Flint, L.E., 1998b. Characterization of Hydrogeologic Units Using Matrix Properties, Yucca Mountain, Nevada. USGS Water Resources Investigation Report 97-4243, Denver, CO.
- Glass, R.J., Nicholl, M.J., Tidwell, V.C., 1995. Challenging models for flow in unsaturated, fractured rock through exploration of small scale flow processes. *Geophys. Res. Lett.* 22 (11), 1457–1460.
- Glass, R.J., Nicholl, M.J., Ramirez, A.L., Daily, W.D., 2002. Liquid phase structure within an unsaturated fracture network beneath a surface infiltration event: field experiment. *Water Resour. Res.* 38 (10), 1199. doi:10.1029/2001WR000167.
- Hinds, J.J., Bodvarsson, G.S., Nieder-Westermann, G.H., 2003. Conceptual evaluation of the potential role of fractures in unsaturated processes at Yucca Mountain. *J. Contam. Hydrol.* 62–63, 111–132.
- Liu, B., Fabryka-Martin, J., Wolfsberg, A., Robinson, B., Sharma, P., 1995. Significance in Apparent Discrepancies in Water Ages Derived From Atmospheric Radionuclides at Yucca Mountain, Nevada. Rep. LA-UR-95-572. Los Alamos Natl. Lab., Los Alamos, NM.
- Liu, H.H., Doughty, C., Bodvarsson, G.S., 1998. An active fracture model for unsaturated flow and transport in fractured rocks. *Water Resour. Res.* 34 (10), 2633–2646.
- Liu, H.H., Bodvarsson, G.S., Finsterle, S., 2002. A note on unsaturated flow in two-dimensional fracture networks. *Water Resour. Res.* 38 (9), 1176. doi:10.1029/2001WR000977.
- Liu, H.H., Zhang, G., Bodvarsson, G.S., 2003a. The active fracture model: its relation to fractal flow patterns and an evaluation using field observations. *Vadose Zone J.* 2, 259–269.
- Liu, H.H., Haukwa, C.B., Ahlers, C.F., Bodvarsson, G.S., Flint, A.L., Guertel, W.B., 2003b. Modeling flow and transport in unsaturated fractured rock: an evaluation of the continuum approach. *J. Contam. Hydrol.* 62–63, 173–188.
- Liu, H.H., Salve, R., Wang, J.S.Y., Hudson, D., 2004. Field investigation into unsaturated flow and transport in a fault: 3. Model analysis. *J. Contam. Hydrol.* 74, 39–59.
- Nativ, R., Adar, E., Dahan, O., Geyh, M., 1995. Water recharge and solute transport through the vadose zone of fractured chalk under desert conditions. *Water Resour. Res.* 31 (2), 253–261.
- Neuman, S.P., 1994. Generalized scaling of permeabilities: validation and effect of support scale. *Geophys. Res. Lett.* 21 (5), 349–352.
- Nicholl, M.J., Glass, R.J., Wheatcraft, S.W., 1994. Gravity-driven infiltration instability in initially dry nonhorizontal fractures. *Water Resour. Res.* 30 (9), 2533–2546.
- NRC (National Research Council), 2001. Conceptual Models of Flow and Transport in the Fractured Vadose Zone. National Academy Press, Washington D.C.
- Ohman, J., Niemi, A., 2003. Upscaling of fracture hydraulics by means of an oriented correlated stochastic continuum model. *Water Resour. Res.* 39 (10), 1277. doi:10.1029/2002WR001776.
- Philip, J.R., 1990. Some general results on the seepage exclusion problem. *Water Resour. Res.* 26 (3), 367–377.
- Pruess, K., 1999. A mechanistic model for water seepage through thick unsaturated zones in fractured rocks of low matrix permeability. *Water Resour. Res.* 35 (4), 1039–1051.



- Pruess, K., Narasimhan, T.N., 1985. A practical method for modeling fluid and heat flow in fractured porous media. *Soc. Pet. Eng. J.* 25, 14–26.
- Pruess, K., Oldenburg, C.M., Moridis, G., 1999. TOUGH2 User's Guide. Report LBNL-43134. Lawrence Berkeley National Laboratory, Berkeley, CA.
- Richards, L.H., 1931. Capillary conduction of liquids through porous mediums. *Physics* 1, 318–333.
- Salve, R., 2005. Observation of preferential flow during a liquid release experiment in fractured welded tuffs. *Water Resour. Res.* 41, W09427. doi:10.1029/2004WR003570.
- Salve, R., Oldenburg, C.M., Wang, J.S.Y., 2003. Fault-matrix interactions in nonwelded tuff of the Paintbrush Group at Yucca Mountain. *J. Contam. Hydrol.* 62–63, 269–286.
- Salve, R., Liu, H.H., Hu, Q., Hudson, D., Cook, P., Czarnomski, A., 2004. Unsaturated flow and transport through a fault embedded in fractured welded tuff. *Water Resour. Res.* 40 (4), W04210. doi:10.1029/2003WR002571.
- Su, G.W., Geller, J.T., Pruess, K., Wen, F., 1999. Experimental studies of water seepage and intermittent flow in unsaturated, rough-walled fractures. *Water Resour. Res.* 35 (4), 1019–1037.
- Therrien, R., Sudicky, E.A., 1996. Three-dimensional analysis of variably-saturated flow and solute transport in discretely-fractured porous media. *J. Contam. Hydrol.* 23, 1–44.
- Tokunaga, T.K., Wan, J., 1997. Water film flow along fracture surfaces of porous rock. *Water Resour. Res.* 33 (6), 1287–1295.
- Trautz, R.C., Wang, J.S.Y., 2002. Seepage into an underground opening constructed in unsaturated fractured rock under evaporative conditions. *Water Resour. Res.* 38 (10), 1188. doi:10.1029/2001WR000690.
- van Genuchten, M.T., 1980. A closed-form equation for predicting the hydraulic conductivity of unsaturated soils. *Soil Sci. Soc. Am. J.* 44, 892–898.
- Wang, J.S.Y., Bodvarsson, G.S., 2003. Evolution of the unsaturated zone testing at Yucca Mountain. *J. Contam. Hydrol.* 62–63, 337–360.
- Wang, J.S.Y., Elsworth, D., 1999. Permeability changes induced by excavation in fractured tuff. *rock mechanics for industry*. In: Amadei, B., Kranz, R.L., Scott, G.A., Smeallie, P.H. (Eds.), *Proceedings of the 37th U.S. Rock Mechanics Symposium*, Vail, Colorado, USA, 6–9 June 1999, vol. 2. A.A. Balkema, Brookfield, Vermont, pp. 751–757.
- Warren, J.E., Root, P.J., 1963. The behavior of naturally fractured reservoirs. *Soc. Pet. Eng. J.* 245–255, *Transactions, AIME*, 228.
- Wealthall, G.P., Steele, A., Bloomfield, J.P., Moss, R.H., Lerner, D.N., 2001. Sediment filled fractures in the Permo-Triassic sandstones of the Cheshire Basin: observations and implications for pollutant transport. *J. Contam. Hydrol.* 50, 41–51.
- Wu, Y.S., Ritcey, A.C., Bodvarsson, G.S., 1999. A modeling study of perched water phenomena in the unsaturated zone at Yucca Mountain. *J. Contam. Hydrol.* 38, 157–184.
- Yang, I.C., Rattay, G.W., Yu, P., 1996. Interpretation of chemical and isotopic data from boreholes in the unsaturated zone at Yucca Mountain, Nevada. *U.S. Geol. Surv. Water Resour. Invest. Rep.* 96-4058, 58 pp.
- Zhou, Q., Gelhar, L.W., Jacobs, B., 2002. Comparison of field-scale effective properties of two-phase flow in heterogeneous porous media obtained by stochastic analysis and numerical experiments. In: Findikakis, A.N. (Ed.), *Proceedings of the International Groundwater Symposium on Bridging the Gap between Measurements and Modeling in Heterogeneous Media*, Berkeley, California, March 25–29, 2002.
- Zhou, Q., Liu, H.H., Bodvarsson, G.S., Oldenburg, C.M., 2003. Flow and transport in unsaturated fractured rock: effects of multiscale heterogeneity of hydrogeologic properties. *J. Contam. Hydrol.* 60, 1–30.
- Zhou, Q., Birkholzer, J.T., Javandel, I., Jordan, P.D., 2004. Modeling three-dimensional groundwater flow and advective contaminant transport at a heterogeneous mountainous site in support of remediation. *Vadose Zone J.* 3, 884–900.
- Zhou, Q., Liu, H.H., Bodvarsson, G.S., Molz, F.J., 2006. Evidence of multi-process matrix diffusion in a single fracture from a field tracer test. *Transp. Porous Media* 63 (3), 473–487.